Supplemental Materials

Molecular Biology of the Cell

Irajizad et al.

Support Information for "Geometric instability catalyzes mitochondrial fission"

Ehsan Irajizad[a], Rajesh Ramachandran[b], and Ashutosh Agrawal[*c]

1 Model description

1.1 Surface geometry

We model a bilayer as a two-dimensional surface ω with a non-uniform distribution of curvature-inducing lipids and proteins. The position vector to an arbitrary point on the surface is given by $\mathbf{r}(\theta^\mu)$, where θ^μ are the surface coordinates. Here and henceforth, Greek indices range over $\{1, 2\}$ and, if repeated, are summed over that range. The basis vectors on the tangent plane are given by $\mathbf{a}_\alpha = \mathbf{r}_{,\alpha}$ which yields the metric $a_{\alpha\beta} = \mathbf{a}_\alpha \cdot \mathbf{a}_\beta$ and the unit surface normal vector $\mathbf{n} = \mathbf{a}_1 \times \mathbf{a}_2 / |\mathbf{a}_1 \times \mathbf{a}_2|$. Here, $()_{,\alpha} = \partial()/\partial\theta^\alpha$. The curvature tensor is given by $\mathbf{b} = b_{\alpha\beta}\mathbf{a}^\alpha \otimes \mathbf{a}^\beta$ where $b_{\alpha\beta} = \mathbf{n} \cdot \mathbf{r}_{,\alpha\beta} = -\mathbf{a}_\alpha \cdot \mathbf{n}_{,\beta}$ are the coefficients of the second fundamental form, $\mathbf{a}^\alpha = a^{\alpha\beta}\mathbf{a}_\beta$ are the contravariant basis vectors, and $(a^{\alpha\beta}) = (a_{\alpha\beta})^{-1}$ is the dual metric Kreyszig (1959). These yield the three curvature invariants on a surface

$$
\begin{aligned}
H &= \frac{1}{2} a^{\alpha\beta} b_{\alpha\beta} = (\kappa_\lambda + \kappa_\mu)/2, \\
K &= \frac{1}{2} \varepsilon^{\alpha\beta} \varepsilon^{\theta\psi} b_{\alpha\theta} b_{\beta\psi} = \kappa_\lambda \kappa_\mu - \tau^2. \\
D &= \frac{1}{2} b_{\alpha\beta} (\lambda^\alpha \lambda^\beta - \mu^\alpha \mu^\beta) = (\kappa_\lambda - \kappa_\mu)/2
\end{aligned}
\tag{1}
$$

where H is the mean curvature, K is the Gaussian curvature and D is the curvature deviator. Above, $\{\kappa_\lambda, \kappa_\mu\}$ are the principal curvatures, τ is the twist, and $\varepsilon^{\alpha\beta} = a^{-\frac{1}{2}} e^{\alpha\beta}$ is the permutation tensor density where $e^{\alpha\beta}$ is the permutation tensor.

1.2 The energy functional and the equilibrium equations

For isotropic membranes, the strain energy W depends only on the mean and the Gaussian curvatures Jenkins (1977); Steigmann (1999). We refer the reader to Deserno (2015) for more details on the theory of membranes. For anisotropic membranes where proteins break the isotropic symmetry and introduce an orthotropic symmetry (invariance under 180° rotation), the strain energy depends on the third invariant- curvature deviator D Fošnaric et al. (2005); Kralj-Iglič et al. (1999, 2002); Walani et al. (2014). For the problem investigated in this study, lipids and proteins have a contrasting effect. The curvature inducing lipids PE and CL generate spherical curvature and preserve isotropy. On the other hand, the Drp1 proteins induce cylindrical curvatures and introduce orthotropic symmetry. For the generalized strain

energy, the total free energy of a bilayer that accounts for the areal and volume constraints is given by

$$E = E_b - E_f \tag{2}$$

where

$$E_f = \int_{\omega_a} \mathbf{f}(\theta^\alpha).(\mathbf{r} - \mathbf{r}_0)da \tag{3}$$

$$E_b = \int_{\omega} (W(H, D, K; \theta^\alpha) + \lambda(\theta^\alpha))da - pV(\omega). \tag{4}$$

where here, f is the force per unit area (applied by actin filaments) on a point on the surface with a position vector r in the current configuration and r_0 in the reference configuration, λ is the surface tension field which is the Lagrange multiplier associated with the local area constraint, p is the transmembrane pressure which is the Lagrange multiplier associated with the volume constraint and V is the enclosed volume.

To derive the stationarity conditions, we consider a general variation

$$\mathbf{u} = u^\alpha \mathbf{a}_\alpha + u\mathbf{n}. \tag{5}$$

where u^α are the tangential variations, and u is the normal variation. As shown in Walani et al. (2014), the tangential variations yield the Euler equation

$$\lambda_{,\eta} = -\partial W/\partial\theta^\eta - W_D(b_{\alpha\beta}(\lambda^\alpha\lambda^\beta)_{;\eta}) - \mathbf{f}.\mathbf{a}_\eta. \tag{6}$$

This equation allows computation of the surface tension field as a function of the surface coordinates. For homogeneous membranes, it is trivially satisfied and yields a constant surface tension value. In the domains where the membrane possesses isotropic symmetry, dependence of W on D is suppressed.

For normal variation, following the procedure outlined in Walani et al. (2014), we derive the so-called *shape equation* that governs the geometry of the membrane

$$\begin{aligned}&\frac{1}{2}[W_D(\lambda^\alpha\lambda^\beta - \mu^\alpha\mu^\beta)]_{;\beta\alpha} + \frac{1}{2}W_D(\lambda^\alpha\lambda^\beta - \mu^\alpha\mu^\beta)b_{\alpha\gamma}b^\gamma_\beta + \Delta(\frac{1}{2}W_H) + (W_K)_{;\beta\alpha}\tilde{b}^{\beta\alpha} \\ &+ W_H(2H^2 - K) + 2H(KW_K - W) - 2H\lambda = p + \mathbf{f}.\mathbf{n}.\end{aligned} \tag{7}$$

1.2.1 Boundary Forces and Moment

The procedure outlined in Agrawal and Steigmann (2009); Walani et al. (2014) also yields the boundary terms from the tangential and the normal variations

$$\dot{E}_B = \int_{\partial\omega} (F_\nu\boldsymbol{\nu} + F_\tau\boldsymbol{\tau} + F_n\mathbf{n}) \cdot \mathbf{u}ds - \int_{\partial\omega} M\boldsymbol{\tau} \cdot \boldsymbol{\omega}ds. \tag{8}$$

where

$$
\begin{aligned}
M &= \frac{1}{2}W_H + \kappa_\tau W_K + W_D\lambda^\alpha\lambda^\beta\nu_\beta\nu_\alpha - \frac{1}{2}W_D,\\
F_\nu &= W + \lambda - \kappa_\nu M,\\
F_\tau &= -\tau M,\\
F_n &= (\tau W_K)' - \frac{1}{2}(W_H)_{,\nu} - (W_K)_{,\beta}\tilde{b}^{\alpha\beta}\nu_\alpha,\\
&+ \frac{1}{2}(W_D)_{,\nu} - (W_D\lambda^\alpha\lambda^\beta)_{;\beta}\nu_\alpha - (W_D\lambda^\alpha\lambda^\beta\nu_\beta\tau_\alpha)'.
\end{aligned}
\tag{9}
$$

Above, M is the bending moment per unit length, F_ν is the in-plane normal force per unit length, F_τ is the in-plane shear force per unit length, F_n is the transverse shear force per unit length, and the edge discontinuities have been neglected.

1.3 Axisymmetric Deformations

We assume that the undeformed and the deformed mitochondria shapes possess axisymmetry. We therefore parametrize the surface by the meridional arc length s and the azimuthal angle θ. For such a surface,

$$
\mathbf{r}(s,\theta) = r(s)\mathbf{e}_r(\theta) + z(s)\mathbf{k} \tag{10}
$$

where $r(s)$ is the radius from axis of revolution, $z(s)$ is the elevation from a base plane and $(\mathbf{e}_r, \mathbf{e}_\theta, \mathbf{k})$ form the coordinate basis. Since $(r')^2 + (z')^2 = 1$, we can define an angle ψ such that

$$
r'(s) = \cos\psi \quad \text{and} \quad z'(s) = \sin\psi. \tag{11}
$$

Above, $()' = \partial()/\partial s$. With $\theta^1 = s$ and $\theta^2 = \theta$, we can easily show that

$$
\begin{aligned}
\mathbf{a}_1 &= r'\mathbf{e}_r + z'\mathbf{k}, \quad \mathbf{a}_2 = r\mathbf{e}_\theta,\\
\mathbf{n} &= -\sin(\psi)\mathbf{e}_r + \cos(\psi)\mathbf{k},
\end{aligned}
\tag{12}
$$

$$
\boldsymbol{\lambda} = -\mathbf{e}_\theta, \quad \boldsymbol{\mu} = \cos\psi\mathbf{e}_r + \sin\psi\mathbf{k}. \tag{13}
$$

Fig. S3a shows the orientations of $\mathbf{n}$, $\boldsymbol{\lambda}$ and $\boldsymbol{\mu}$. In the axisymmetric setting, the normal curvatures are given by $\kappa_\lambda = (\sin\psi)/r$ and $\kappa_\mu = \psi'$ which then yield the curvature invariants

$$
\begin{aligned}
2H &= \frac{\sin\psi}{r} + \psi',\\
K &= H^2 - (H - (\sin\psi)/r)^2, \quad \text{and}\\
D &= [(\sin\psi)/r - \psi']/2.
\end{aligned}
\tag{14}
$$

Using these expressions, the Euler-Lagrange equations for an axisymmetric geometry reduce to

$$
\lambda' = -W' - \mathbf{f}.\mathbf{a}_1. \tag{15}
$$

and

$$p + \mathbf{f}.\mathbf{n} = \frac{L'}{r} + W_H(2H^2 - K) - 2H(W + \lambda - W_D D) + \frac{((W_D)' \cos\psi)}{r} \tag{16}$$

where

$$L/r = \frac{1}{2}[(W_H)' - (W_D)']. \tag{17}$$

In the above equations, we suppress the dependence on D in the isotropic domains.
For an axisymmetric case, we can express the strain energy density in terms of curvatures along principal directions $\{\kappa_\lambda, \kappa_\mu\}$

$$W = \hat{k}_1(\kappa_\lambda - \kappa_\lambda^0)^2 + \hat{k}_2(\kappa_\mu - \kappa_\mu^0)^2 + 2\hat{k}_{12}(\kappa_\lambda - \kappa_\lambda^0)(\kappa_\mu - \kappa_\mu^0). \tag{18}$$

The bending moduli in the $\{H, D\}$ and the $\{\kappa_\lambda, \kappa_\mu\}$ framework are related by the following expressions $\hat{k}_1 = \hat{k}_2 = (\hat{K}_1 + \hat{K}_2)$ and $\hat{k}_{12} = (\hat{K}_1 - \hat{K}_2)$. In order to maintain a control over the domains over which PE and Drp1 proteins interact with the membrane, we transform the independent variable from arclength s to area a with the help of the relation $da/ds = 2\pi r$.

In addition, we use the radius of the initial spherocylinder R_0 to non-dimensionalize the system of equations. The non-dimensional variables are given by

$$\begin{aligned}
&\bar{r} = r/R_0,\ \bar{z} = z/R_0,\ \ \bar{a} = a/2\pi {R_0}^2,\ \bar{\kappa}_\lambda = R_0\kappa_\lambda,\ \bar{W} = W {R_0}^2/k_0,\\
&\bar{\kappa}_\mu = R_0\kappa_\mu,\ \bar{H} = R_0 H,\ \bar{D} = R_0 D,\ \bar{K} = {R_0}^2 K,\ \bar{\lambda} = \lambda {R_0}^2/k_0,\\
&\bar{L} = R_0 L/k_0,\ \bar{k}_1 = \hat{k}_1/k_0,\ \bar{k}_2 = \hat{k}_2/k_0,\ \bar{p} = p{R_0}^3/k_0, \bar{\mathbf{f}} = {R_0}^3/k_0 \mathbf{f}.
\end{aligned} \tag{19}$$

In terms of these normalized parameters and the partial derivative with respect to a, $\mathring{()} = \partial()/\partial\bar{a}$, the system of equations can be written as

$$\mathring{\bar{r}} = \cos\psi/\bar{r}, \qquad \mathring{\bar{z}} = \sin\psi/\bar{r}, \tag{20}$$

$$\mathring{\psi} = \bar{\kappa}_\lambda/\bar{r}, \tag{21}$$

$$\bar{L}/\bar{r}^2 = \frac{1}{2}(\mathring{\bar{W}}_H - \mathring{\bar{W}}_D), \tag{22}$$

$$\mathring{\bar{L}} = \bar{p} + \bar{\mathbf{f}}.\mathbf{n} - \bar{W}_H(2\bar{H}^2 - \bar{K}) + 2\bar{H}(\bar{W} + \bar{\lambda} - \bar{W}_D\bar{D}) - \mathring{\bar{W}}_D\cos\psi, \quad \text{and} \tag{23}$$

$$\mathring{\bar{\lambda}} = -\mathring{\bar{W}} - \bar{\mathbf{f}}.\mathbf{a}_1/\bar{r}. \tag{24}$$

In terms of the normalized principal curvatures, Eqs. (22)-(24) can be expressed as

$$\mathring{\bar{L}} = \Big(\bar{p} + \bar{\mathbf{f}}.\mathbf{n} + (\bar{\kappa}_\lambda + \bar{\kappa}_\mu)(W + \bar{\lambda}) - 2\bar{\kappa}_\lambda^2[\bar{k}_1(\bar{\kappa}_\lambda - \bar{\kappa}_\lambda^0) + \bar{k}_{12}(\bar{\kappa}_\mu - \bar{\kappa}_\mu^0)] - 2\bar{\kappa}_\mu^2[\bar{k}_{12}(\bar{\kappa}_\lambda - \bar{\kappa}_\lambda^0) + \bar{k}_2(\bar{\kappa}_\mu - \bar{\kappa}_\mu^0)]\Big) - \mathring{W}_D \cos\psi, \tag{25}$$

$$\mathring{\bar{\kappa}}_\lambda = \frac{(\cos\psi)\bar{\kappa}_\mu}{\bar{r}^2} - \frac{(\sin\psi\cos\psi)}{\bar{r}^3}, \tag{26}$$

$$\begin{aligned}\mathring{\bar{\lambda}} = -\Big(&\mathring{\bar{k}}_1(\bar{\kappa}_\lambda - \bar{\kappa}_\lambda^0)^2 - 2\bar{k}_1(\bar{\kappa}_\lambda - \bar{\kappa}_\lambda^0)\mathring{\bar{\kappa}}_\lambda^0 + \mathring{\bar{k}}_2(\bar{\kappa}_\mu - \bar{\kappa}_\mu^0)^2 - 2\bar{k}_2(\bar{\kappa}_\mu - \bar{\kappa}_\mu^0)\mathring{\bar{\kappa}}_\mu^0 \\ &+ 2\mathring{\bar{k}}_{12}(\bar{\kappa}_\lambda - \bar{\kappa}_\lambda^0)(\bar{\kappa}_\mu - \bar{\kappa}_\mu^0) - 2\bar{k}_{12}(\bar{\kappa}_\mu - \bar{\kappa}_\mu^0)\mathring{\bar{\kappa}}_\lambda^0 - 2\bar{k}_{12}(\bar{\kappa}_\lambda - \bar{\kappa}_\lambda^0)\mathring{\bar{\kappa}}_\mu^0\Big) - \bar{\mathbf{f}}.\mathbf{a}_1/\bar{r}.\end{aligned} \tag{27}$$

Above,

$$\mathring{W}_D = (2\mathring{\bar{k}}_1 - 2\mathring{\bar{k}}_{12})(\bar{\kappa}_\lambda - \bar{\kappa}_\lambda^0) + (2\bar{k}_1 - 2\bar{k}_{12})(\mathring{\bar{\kappa}}_\lambda - \mathring{\bar{\kappa}}_\lambda^0) + (2\mathring{\bar{k}}_{12} - 2\mathring{\bar{k}}_2)(\bar{\kappa}_\mu - \bar{\kappa}_\mu^0) + (2\bar{k}_{12} - 2\bar{k}_2)(\mathring{\bar{\kappa}}_\mu - \mathring{\bar{\kappa}}_\mu^0), \tag{28}$$

and

$$\mathring{\bar{\kappa}}_\mu = \frac{\bar{L}}{2\bar{k}_2\bar{r}^2} + \mathring{\bar{\kappa}}_\mu^0 - \frac{\mathring{\bar{k}}_2}{k_2}(\bar{\kappa}_\mu - \bar{\kappa}_\mu^0) - \frac{\bar{k}_{12}}{k_2}(\mathring{\bar{\kappa}}_\lambda - \mathring{\bar{\kappa}}_\lambda^0) - \frac{\mathring{\bar{k}}_{12}}{k_2}(\bar{\kappa}_\lambda - \bar{\kappa}_\lambda^0). \tag{29}$$

The expressions for the boundary forces and moments reduce to:

$$\begin{aligned} F_\tau &= -\tau M = 0, \\ \bar{M} &= 2\bar{k}_2(\bar{\kappa}_\mu - \bar{\kappa}_\mu^0) + 2\bar{k}_{12}(\bar{\kappa}_\lambda - \bar{\kappa}_\lambda^0), \\ F_\nu &= W + \lambda - \bar{\kappa}_\mu(2\bar{k}_2(\bar{\kappa}_\mu - \kappa_\mu^0) + 2\bar{k}_{12}(\bar{\kappa}_\lambda - \bar{\kappa}_\lambda^0)), \\ \bar{F}_\nu &= \bar{k}_1(\bar{\kappa}_\lambda - \bar{\kappa}_\lambda^0)^2 + \bar{k}_2(\bar{\kappa}_\mu - \bar{\kappa}_\mu^0)^2 + 2\bar{k}_{12}(\bar{\kappa}_\lambda - \bar{\kappa}_\lambda^0)(\bar{\kappa}_\mu - \bar{\kappa}_\mu^0) + \bar{\lambda} - \bar{\kappa}_\mu(2\bar{k}_2(\bar{\kappa}_\mu - \bar{\kappa}_\mu^0) \\ &\quad + 2\bar{k}_{12}(\bar{\kappa}_\lambda - \bar{\kappa}_\lambda^0)), \\ \bar{F}_n &= -\bar{L}/\bar{r}. \end{aligned} \tag{30}$$

1.4 Simulation procedure:

We solve six simultaneous ODE's (20), (21), (25), (26), and (27) to compute the shape of the mitochondria. We prescribe six boundary conditions at the two ends of the simulation domain as shown in Fig. S3b.

i) At the pole of the spherocylinder ($\bar{a} = 0$)

$$\bar{r} = 0, \quad \psi = 0 \quad \text{and} \quad \bar{L} = 0 \tag{31}$$

ii) At the equatorial plane passing through the middle of the spherocylinder ($\bar{a} = \bar{a}_0$)

$$\bar{z} = 0, \quad \psi = \frac{\pi}{2} \quad \text{and} \quad \bar{L} = 0, \tag{32}$$

The ODE's along with the boundary conditions are solved in Matlab using 'bvp4c solver'. For simulating the fission process, we start from an undeformed spherocylinder as the initial shape (Fig. S6a). The initial spherocylinder has a higher curvature at the poles and lower curvature in the middle as shown in Fig. S6b.

The entire shape transition is obtained in 3 steps:
1) ER/Actin-lipid phase: ER/Actin apply force onto the membrane. (Fig. S6a, magenta domain). Since the orientation of the force is not yet established, we assume $\alpha = 0°$ and $\alpha = 45°$. Th results for $\alpha = 45°$ are presented in the main paper, while the results for $\alpha = 0°$ have been presented in Fig. S4. During squeezing, we have assume aggregation of conical lipids in the vicinity of actin domain. Since conical lipids generate spherical curvatures, we increase the curvatures in the longitudinal (κ_λ) and circumferential (κ_ν) directions. We further assume that the total amount of PE is constant. As a result, an increase in the PE concentration in one region leads to a decrease in the PE concentration in the other regions (Figs. S6b,d,f,h,j). For the simulations presented in Fig. 3, we have assumed that the actin force increases linearly from 0 pN to 1.573 pN and the lipid curvature increases linearly from 0.002 nm^{-1} to 0.0035 nm^{-1}. During the depolymerization phase, the actin force is gradually reduced back to 0 pN while the lipid curvature is held constant (Fig. 3b-4 and Fig. S4-4).
2) Drp1-lipid phase: Drp1 forms a cylindrical coat around the membrane tubule and squeezes it. To model this effect, we increase the stiffness, area and curvature of the protein coat linearly during the polymerization phase. The protein stiffness is changed from 0 to $14.5k_BT$, area is changed from 0% to 1.3% of the total area, and the circumferential curvature is changed from 0.0155 nm^{-1} (curvature of the tubule at the initiation of Drp1 polymerization) to 0.0168 nm^{-1}. As before, we assume that the lipid concentration increases linearly during the protein polymerization phase. We therefore increase the lipid curvature (in the blue domain) from 0.0035 nm^{-1} to 0.0046 nm^{-1} (Fig. S6f). In addition, since Drp1 polymerization is known to sequester CL underneath, we prescribe CL-induced (negative) curvature in the Drp1-coated domain linearly from 0.00175 nm^{-1} to 0.0023 nm^{-1}. We then split the Drp1 coat and increase the separation between the two domains. The lipid curvatures and CL curvatures are assumed to remain unchanged in the adjacent blue domains and underneath of bar protein (Fig. S6h shows the final curvatures).
3) Dynamin 2 effect: We also model Dynamin as a cylindrical protein coat around the membrane tubule (similar to Drp1). As for Drp1, we have linearly increased the circumferential curvature, stiffness and area in the center of the tubule. The final values for these three

parameters are 0.15 nm^{-1}, 12 k_BT and 0.35% of the total area, respectively. The lipid curvatures are held fixed and the in-plane stress (F_ν) is calculated using Eq. 30.

References

Agrawal, A. and Steigmann, D. J. (2009), 'Boundary-value problems in the theory of lipid membranes', *Continuum Mechanics and Thermodynamics* **21**(1), 57–82.

Deserno, M. (2015), 'Fluid lipid membranes: From differential geometry to curvature stresses', *Chemistry and physics of lipids* **185**, 11–45.

Fošnaric, M., Bohinc, K., Gauger, D. R., Iglic, A., Kralj-Iglic, V. and May, S. (2005), 'The influence of anisotropic membrane inclusions on curvature elastic properties of lipid membranes', *Journal of chemical information and modeling* **45**(6), 1652–1661.

Jenkins, J. T. (1977), 'The equations of mechanical equilibrium of a model membrane', *SIAM Journal on Applied Mathematics* **32**(4), 755–764.

Kralj-Iglič, V., Heinrich, V., Svetina, S. and Žekš, B. (1999), 'Free energy of closed membrane with anisotropic inclusions', *The European Physical Journal B-Condensed Matter and Complex Systems* **10**(1), 5–8.

Kralj-Iglič, V., Remškar, M., Vidmar, G., Fošnarič, M. and Iglič, A. (2002), 'Deviatoric elasticity as a possible physical mechanism explaining collapse of inorganic micro and nanotubes', *Physics Letters A* **296**(2), 151–155.

Kreyszig, E. (1959), 'Differential geometry'.

Renner, L. D. and Weibel, D. B. (2011), 'Cardiolipin microdomains localize to negatively curved regions of escherichia coli membranes', *Proceedings of the National Academy of Sciences* **108**(15), 6264–6269.

Steigmann, D. (1999), 'Fluid films with curvature elasticity', *Archive for Rational Mechanics and Analysis* **150**(2), 127–152.

Walani, N., Torres, J. and Agrawal, A. (2014), 'Anisotropic spontaneous curvatures in lipid membranes', *Physical Review E* **89**(6), 062715.

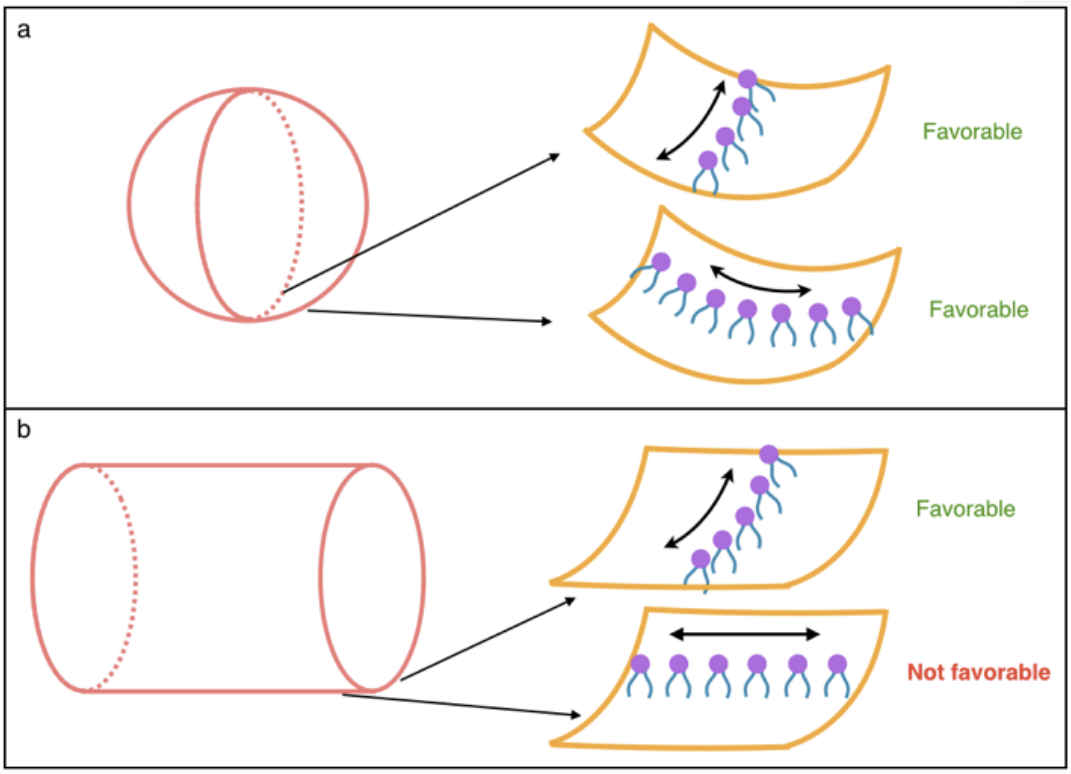

Figure S1: Spherical vs cylindrical curvature from conical lipids. a) If we look at any two orthogonal directions at any point on a sphere, the surface curves the same way. As a result the headgroup area is reduced in all the directions. b) In contrast, if we look at the circumferential and the longitudinal directions at any point on a cylinder, we observe a difference. The headroup area is reduced in the circumferential direction, but remains unchanged in the longitudinal direction. As a result, cone-shaped lipids experience higher exposure to water. For this reason, cone-shaped lipids will have a natural preference for the spherical shape as compared to the cylindrical shape.

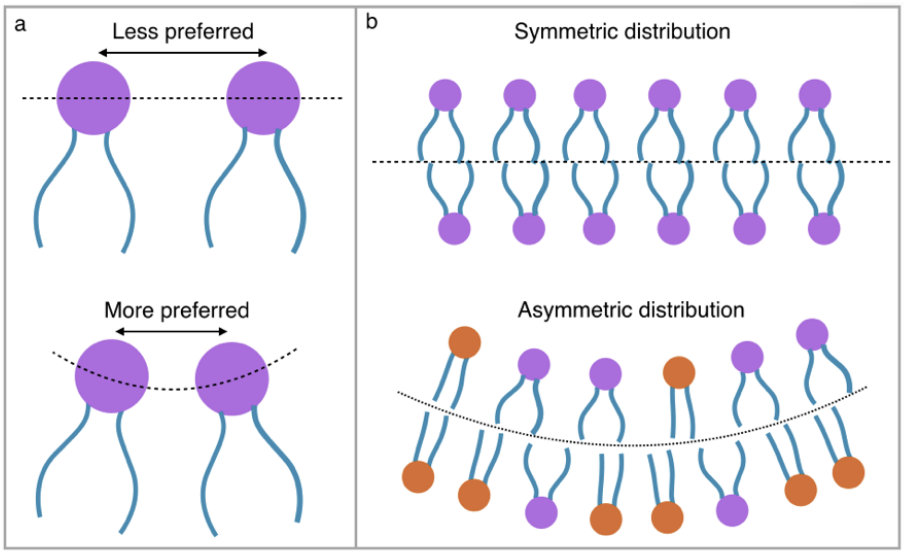

Figure S2: a) Conical lipids prefer a curved leaflet. b) A symmetric distribution of conical lipids in the two leaflets results in a flat bilayer. However, when the conical lipids have asymmetric distribution, a curved configuration becomes the natural state of the bilayer.

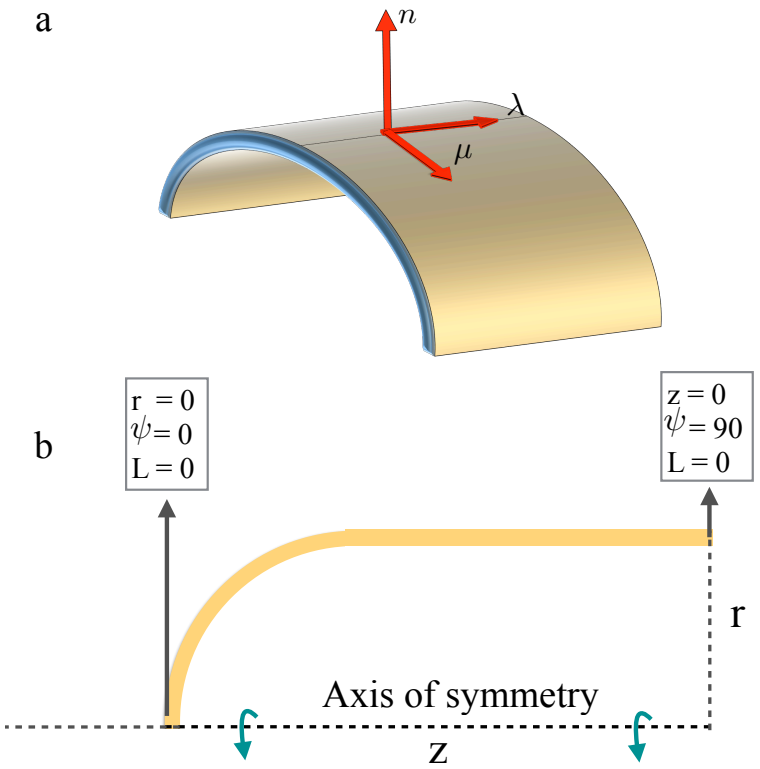

Figure S3: a) The orientation of the three vectors $\mathbf{n}$, $\boldsymbol{\lambda}$ and $\boldsymbol{\mu}$ on a cylindrical surface. b) The prescribed boundary conditions at the two ends of the simulated domain. Due to reflection symmetry, only half the spherocylinder is simulated.

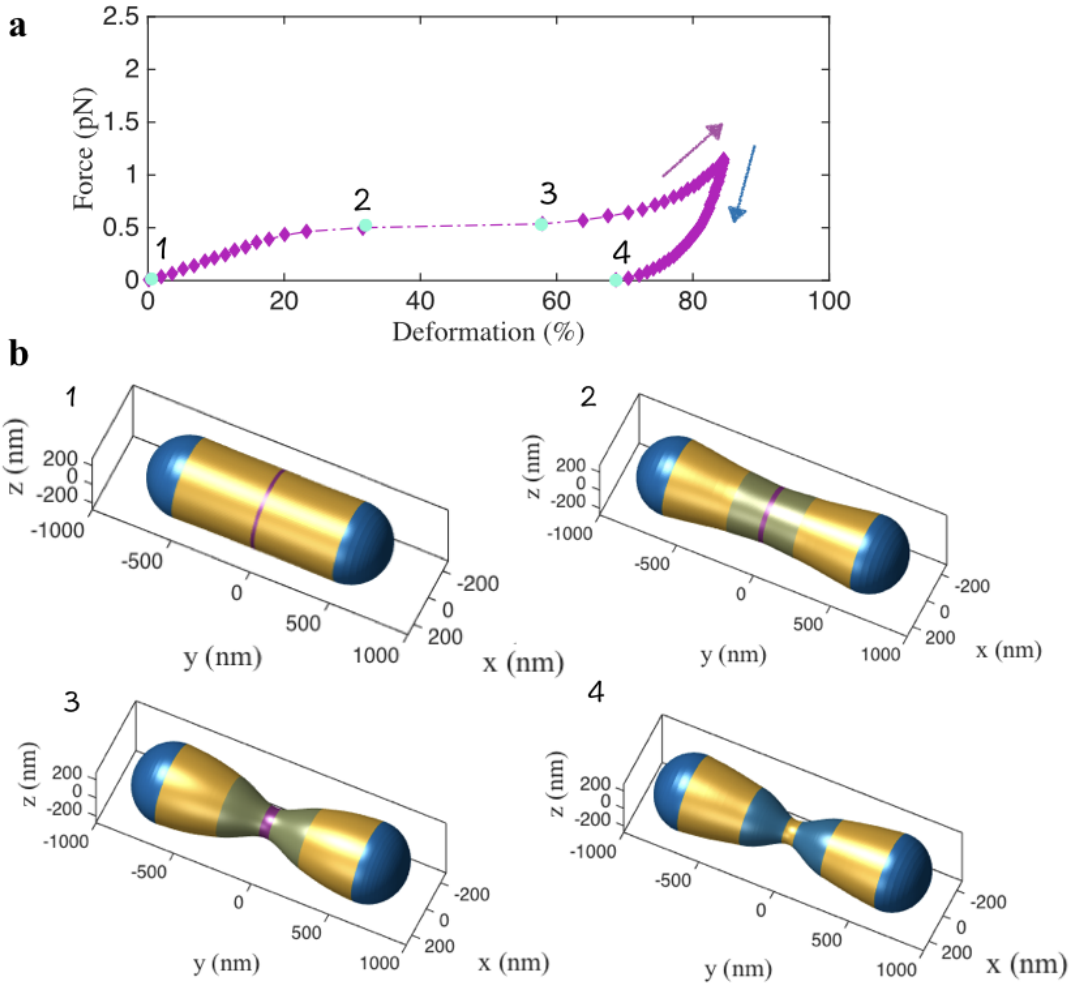

Figure S4: a) The force-deformation response for radially inwards acting actin force ($\alpha = 0^o$). b) The computed shapes during the force-deformation response.

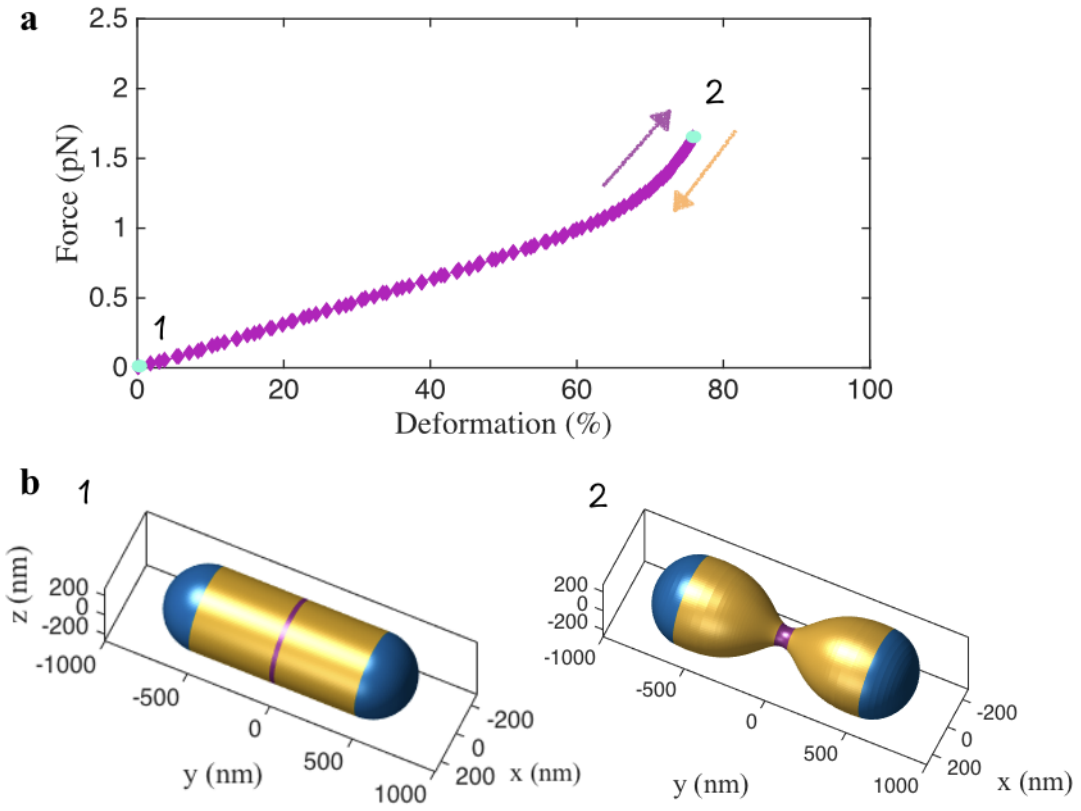

Figure S5: The force-deformation curve generated by actin force in the absence of lipid localization. The deformation response is completely elastic reverting back to the undeformed configuration upon removal of actin force. b) The computed shapes during the force-deformation response.

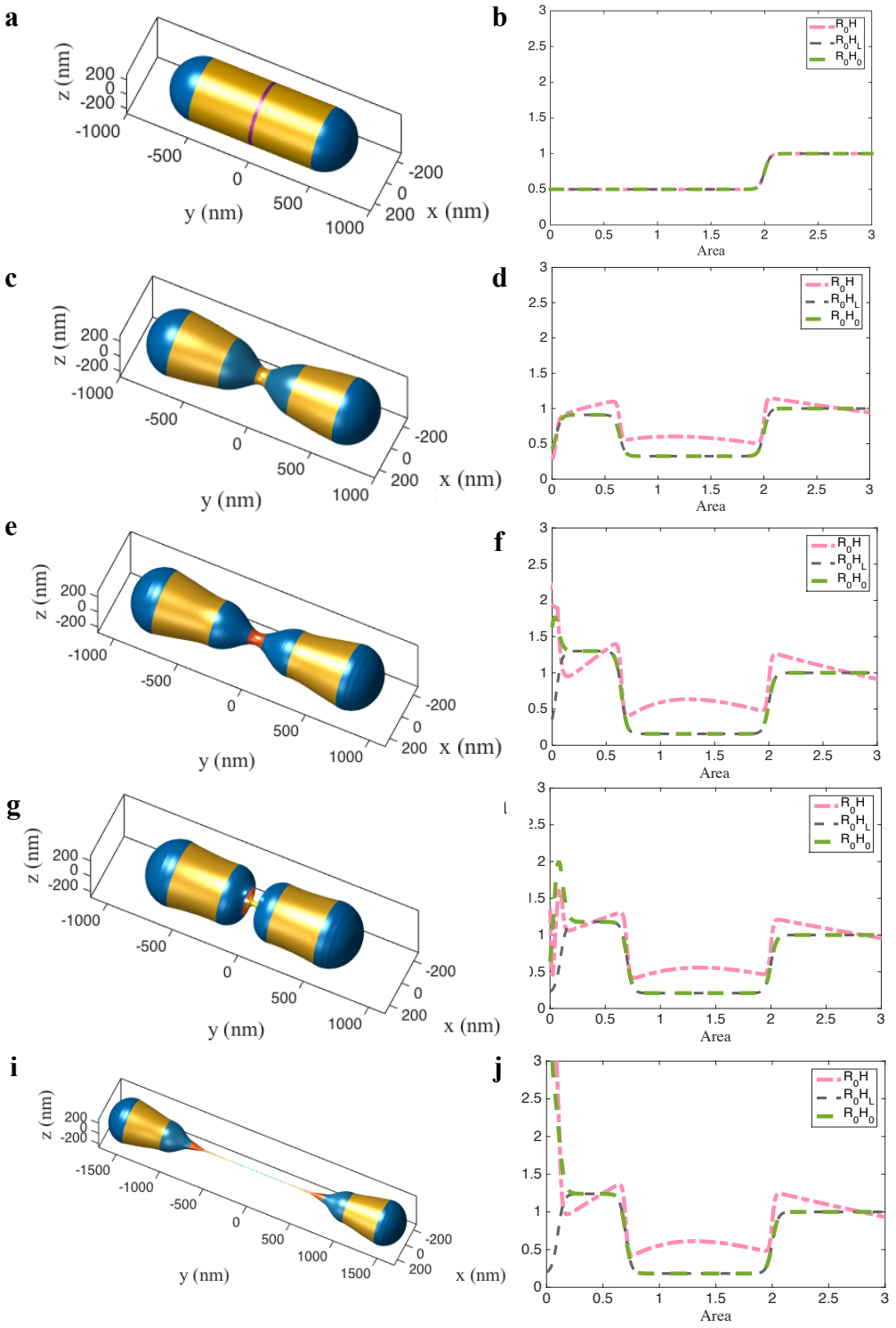

Figure S6: The simulated shape transition for mitochondria fission. a and b) The initial geometry and the corresponding curvature profiles. c and d) The geometry and the corresponding curvature profiles in the presence of ER/Actin force and lipid localization. e and f) The geometry prior to Drp1 splitting and the corresponding curvature profiles. g and h) The final geometry after second instability and the corresponding curvature profiles. i and j) The final squeezed shape due to Dynamin 2 and the corresponding curvature profiles. H is the mean curvature of the surface, H_L is the spontaneous curvature induced by the lipids and H_0 is the total spontaneous curvature from the lipids and the proteins.

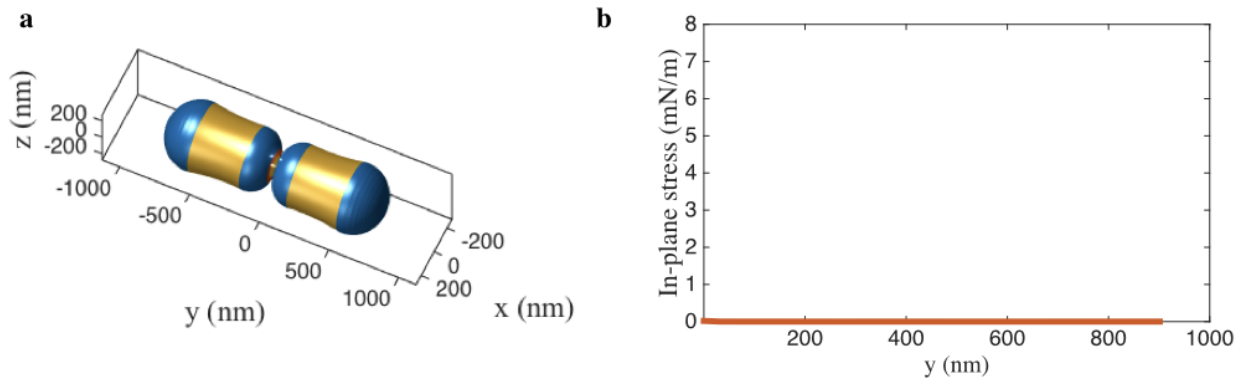

Figure S7: a) A super constriction of 5 nm obtained with higher lipid concentration post Drp1-lipid instability. a) The shape after instability. b) Corresponding *in-plane* stress profile. In comparison to the Dynamin 2 induced squeezing, the in-plane stress remains negligible despite extreme curvatures.

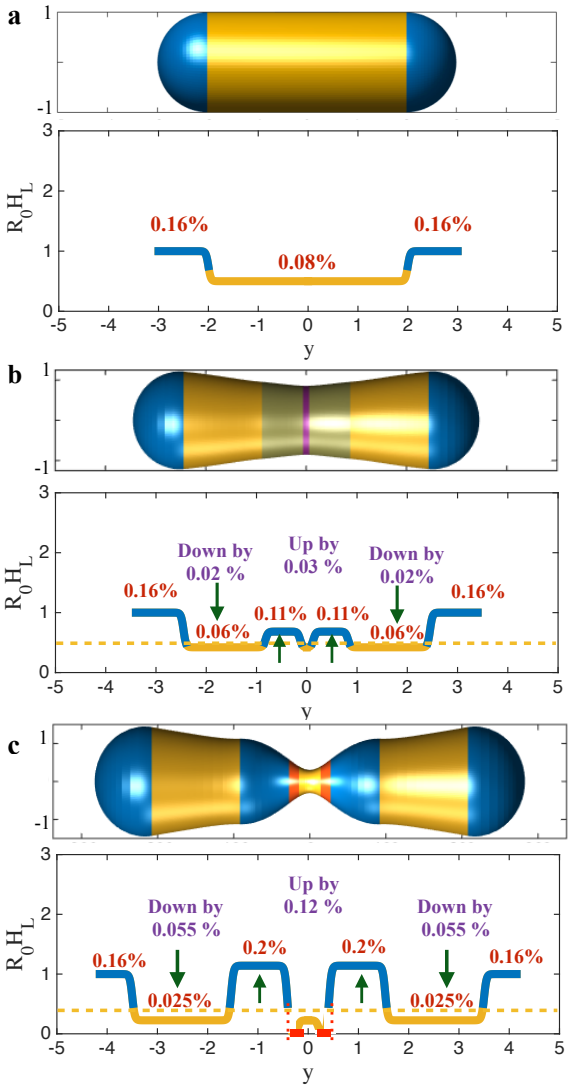

Figure S8: Cardiolipin concentrations. a) The initial geometry and the required CL concentrations. For a tubule radius of 250 nm and CL lipid radius of curvature of 0.4 nm Renner and Weibel (2011), the required (asymmetric) concentration is 0.16% in the hemishperical domain and 0.08% in the cylindrical domain.b) The geometry prior to actin-lipid induced instability and the required CL concentrations. Only 0.03% change in the CL concentration is required in the domain adjacent to actin to trigger the instability. This increase is accompanied by a concomitant decrease in the PE concentration by 0.02% in the cylindrical domain. c) The geometry prior to Drp1-lipid induced instability and the required CL concentrations. Only 0.12% change in the CL concentration is required in the domain adjacent to Drp1 to trigger the instability. This increase is accompanied by a concomitant decrease in the CL concentration by 0.055% in the cylindrical domain. These small changes in the areal concentration are sufficient to achieve extreme necking. It is important to note that the required CL lipids into the central blue domains can come from the nearby yellow domains and are not required to come from the blue domains at the poles. Thus, local rearrangement by $\sim 0.1\%$ adjacent to the protein domain is enough to generate necking conducive for fission.

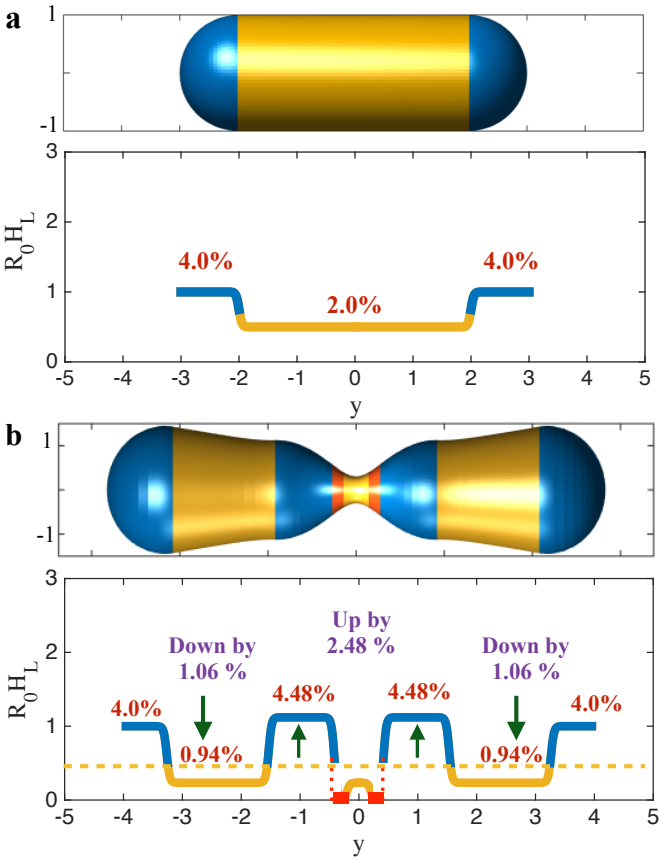

Figure S9: Lipid concentrations for the *in vitro* study. a) The initial geometry and the required PE concentrations. b) The geometry prior to Drp1-lipid induced instability and the required PE concentrations. Only 2.48% change in the PE concentration is required in the domain adjacent to Drp1 to trigger the instability. This increase is accompanied by a concomitant decrease in the PE concentration by 0.94% in the cylindrical domain.

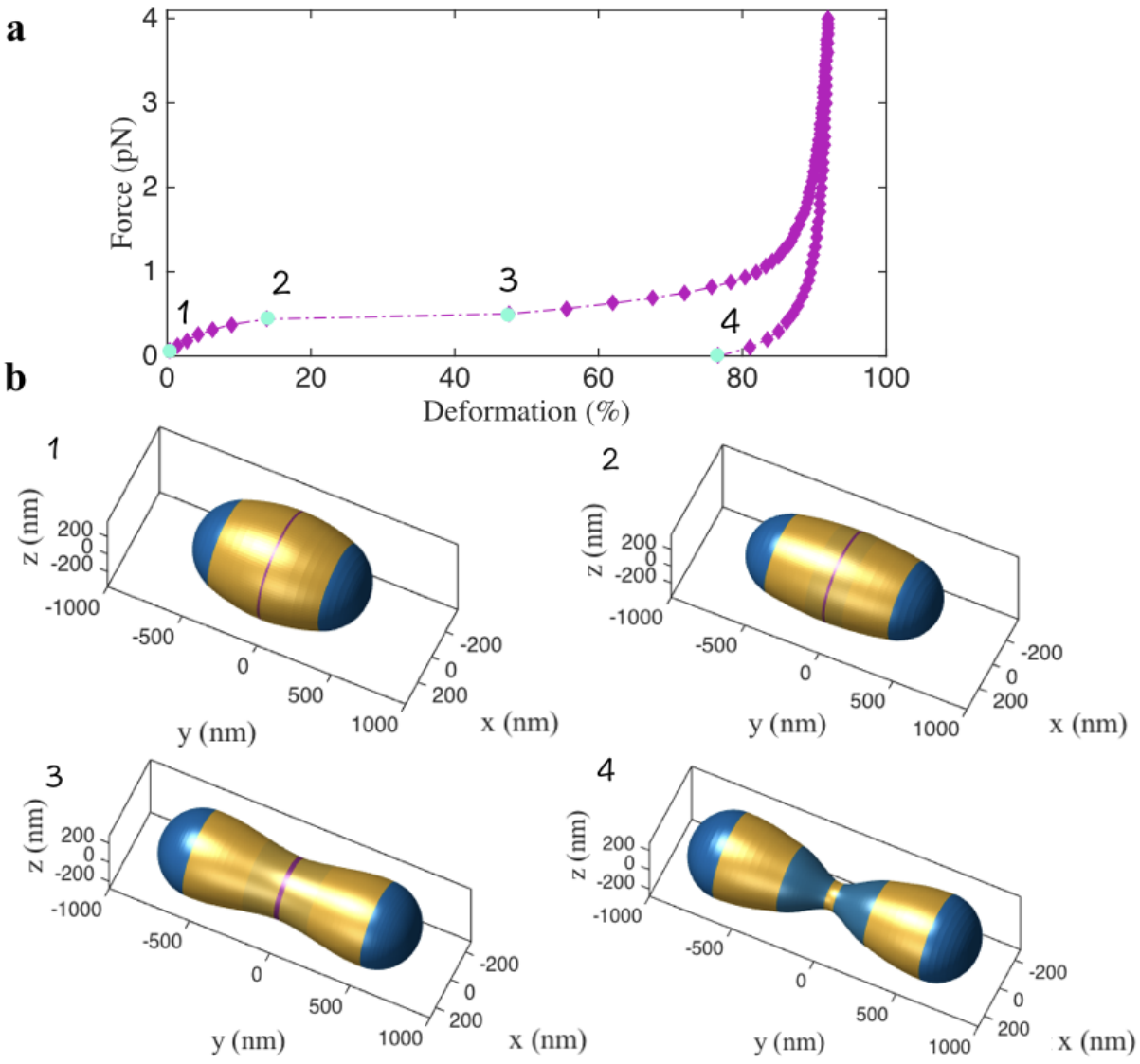

Figure S10: Actin-lipid cooperativity in a mitochondrion with an aspect ratio ($L_0/2R_0$) of 1.5. a) The force-deformation response reveals a similar instability as for a spherocylinder with an aspect ratio of 3 discussed in the main manuscript. b) The computed shapes during the force-deformation response.

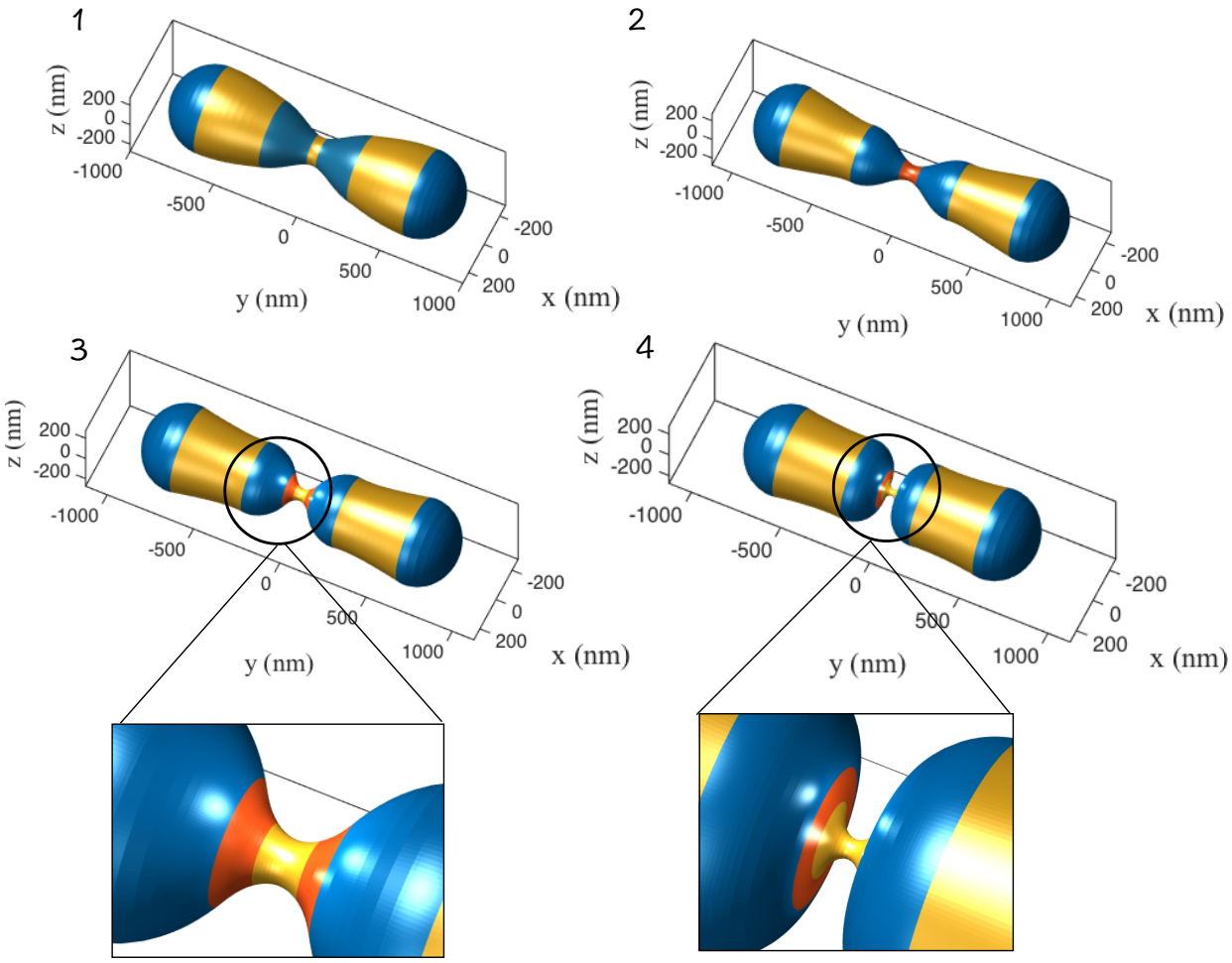

Figure S11: Drp1-lipid cooperativity in a mitochondrion with an aspect ratio ($L_0/2R_0$) of 1.5. The computed shapes during the polymerization and the splitting phases reveal a similar instability as for a spherocylinder with an aspect ratio of 3 discussed in the main manuscript.

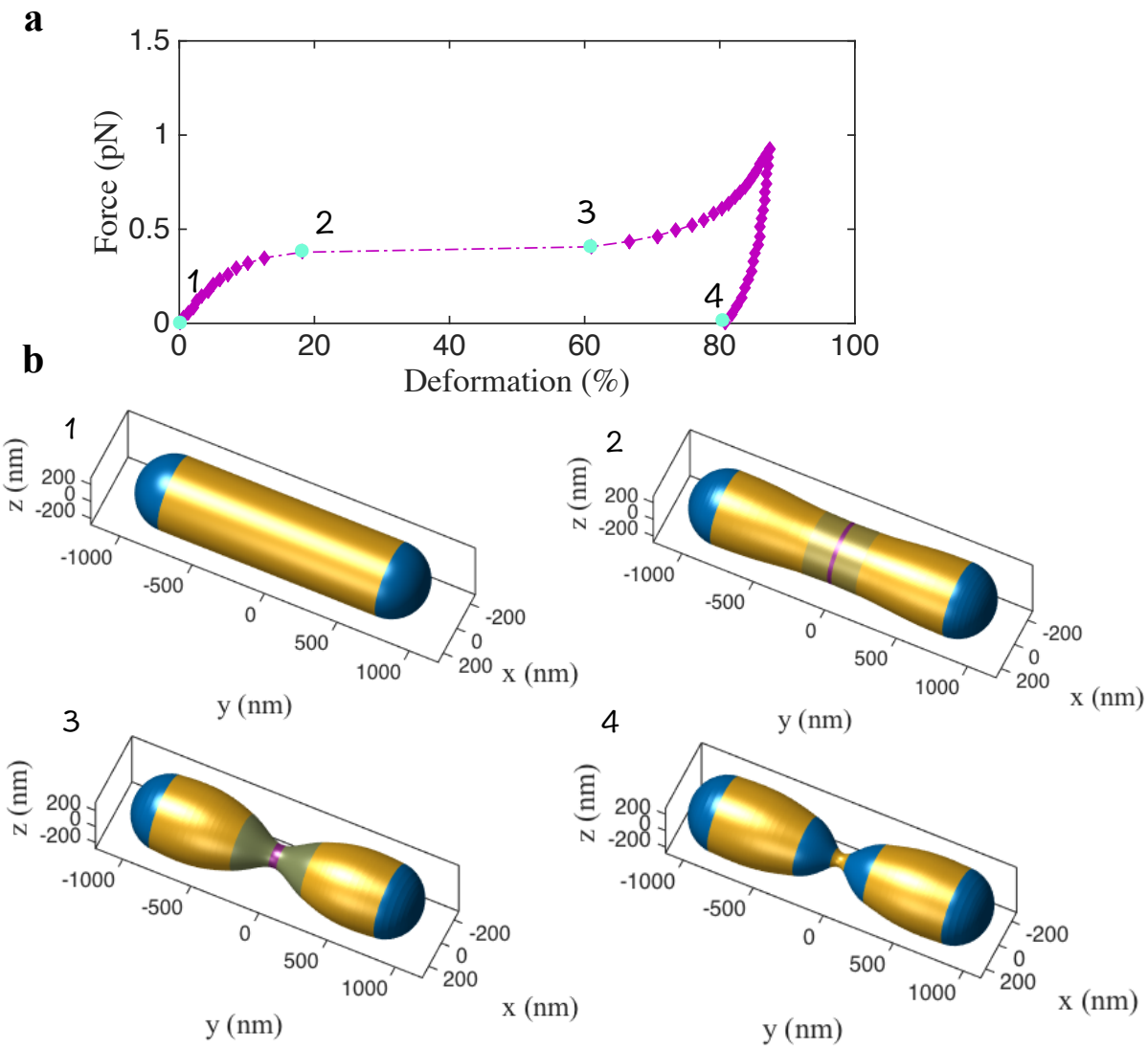

Figure S12: Actin-lipid cooperativity in a mitochondrion with an aspect ratio ($L_0/2R_0$) of 4. a) The force-deformation response reveals a similar instability as for a spherocylinder with an aspect ratio of 3 discussed in the main manuscript. b) The computed shapes during the force-deformation response.

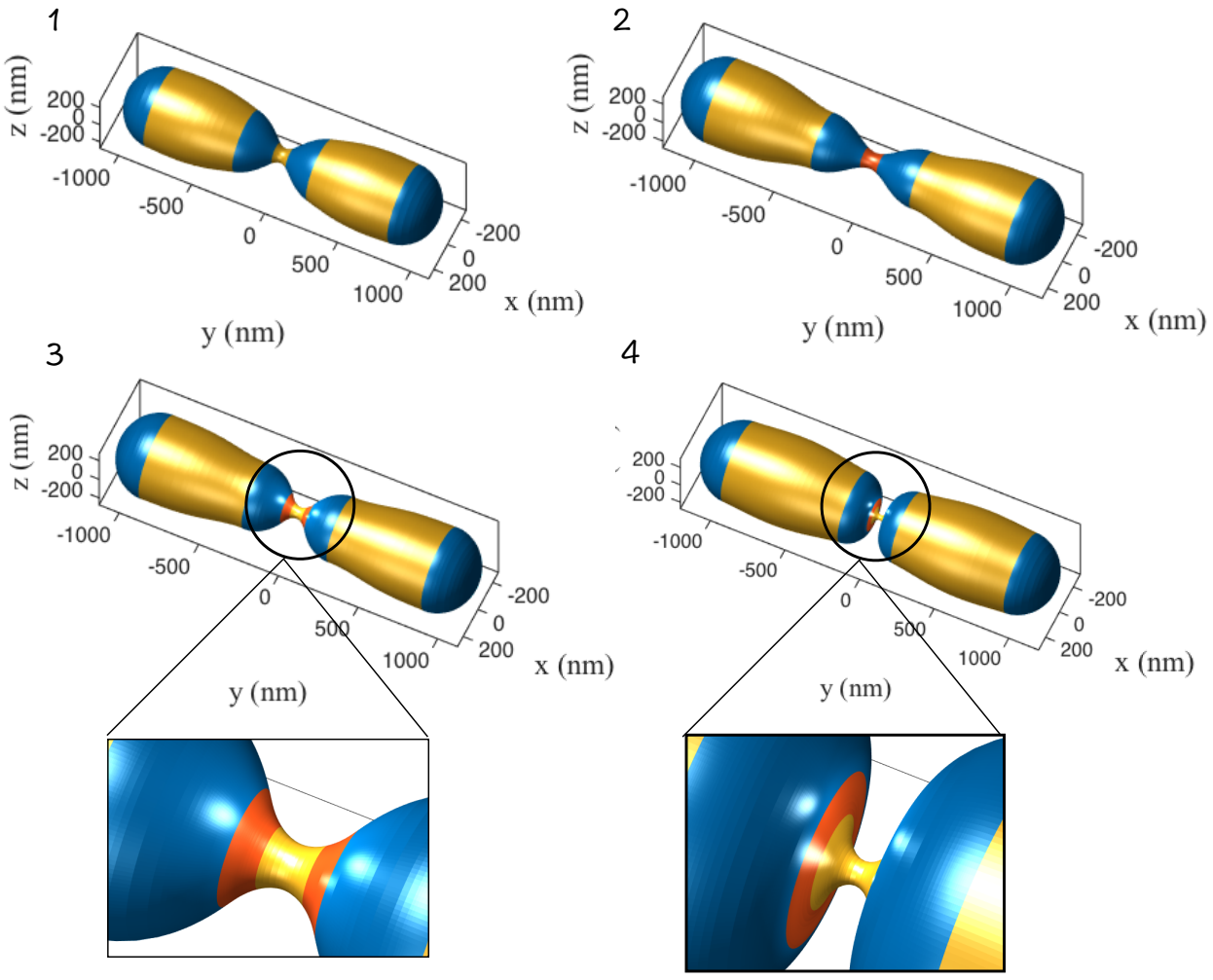

Figure S13: Drp1-lipid cooperativity in a mitochondrion with an aspect ratio ($L_0/2R_0$) of 4. The computed shapes during the polymerization and the splitting phases reveal a similar instability as for a spherocylinder.

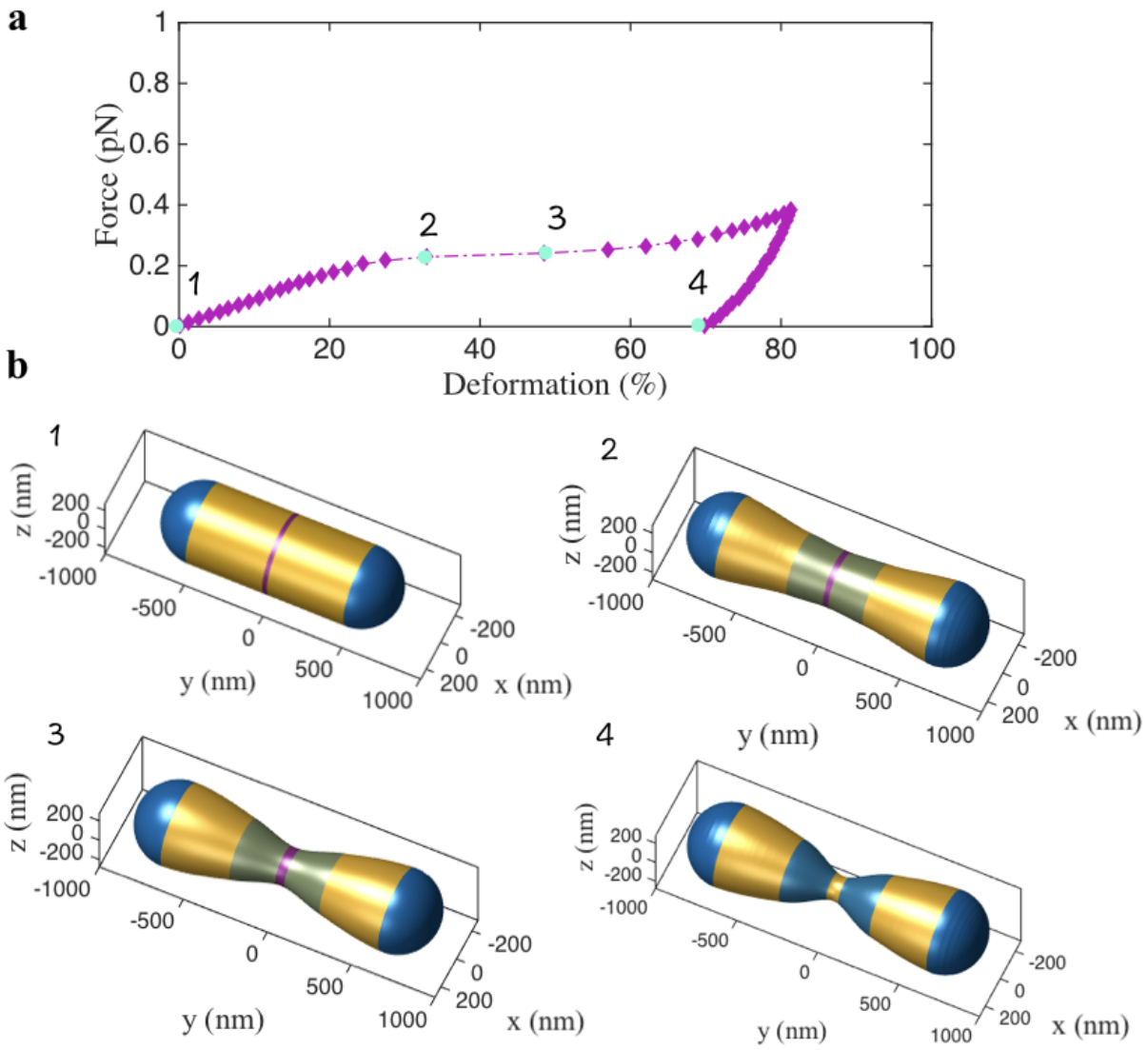

Figure S14: Actin-lipid cooperativity is explored in the presence of an increase in the PE concentration in the blue domains but in the absence of lipid redistribution in the cylindrical domain. This local change in the PE concentration would occur as a result of lipid exchange between the two bilayer leaflets. In the main paper, an increase in the PE concentration in the blue domains results in a concomitant decrease in the cylindrical region, implying global reorganization. a) The force-deformation response again reveals an instability. b) The computed shapes during the force-deformation response.

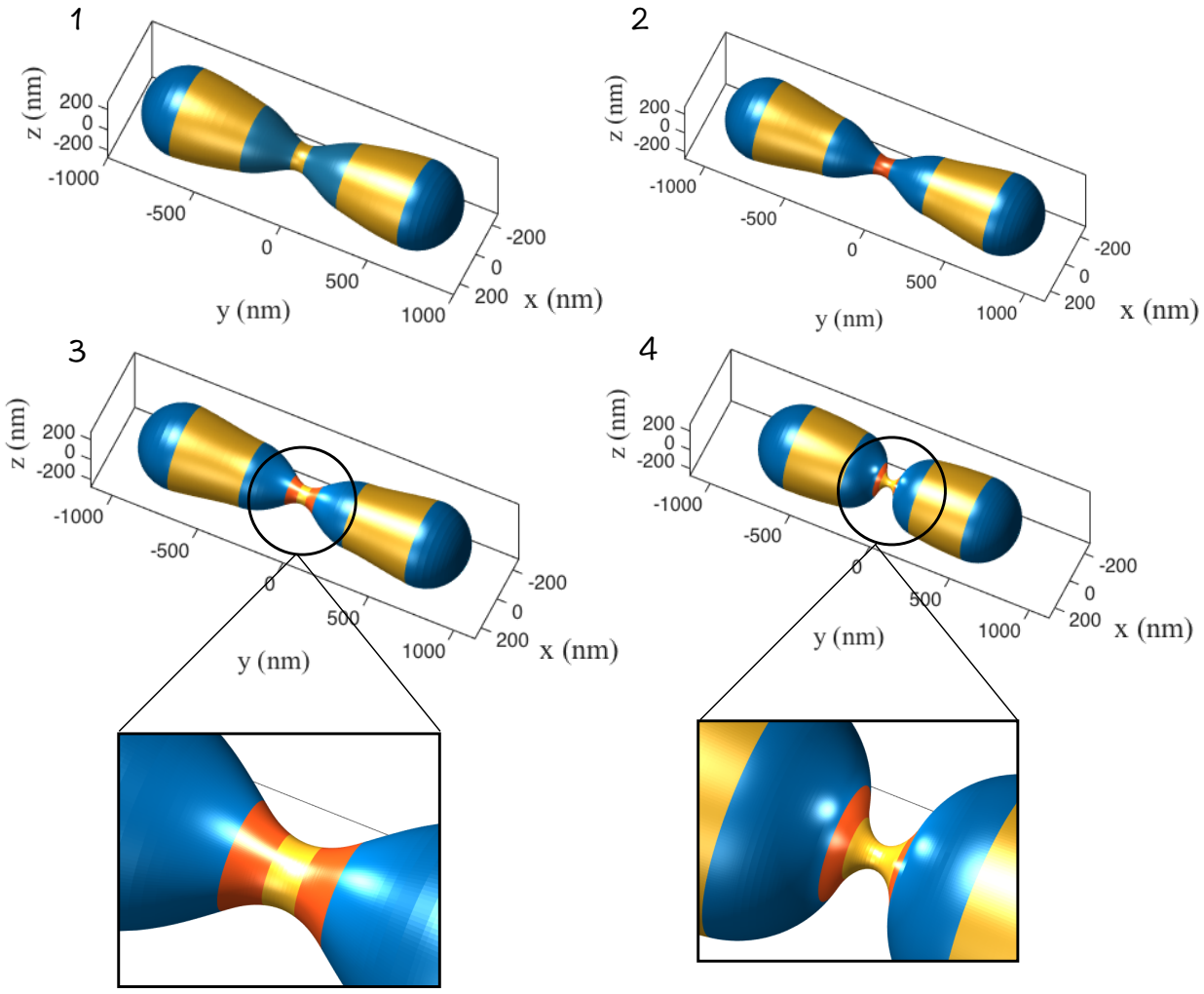

Figure S15: Drp1-lipid cooperativity is explored in the presence of an increase in the PE concentration in the blue domains but in the absence of lipid redistribution in the cylindrical domain. The computed shapes during the polymerization and splitting phases again reveal an instability.

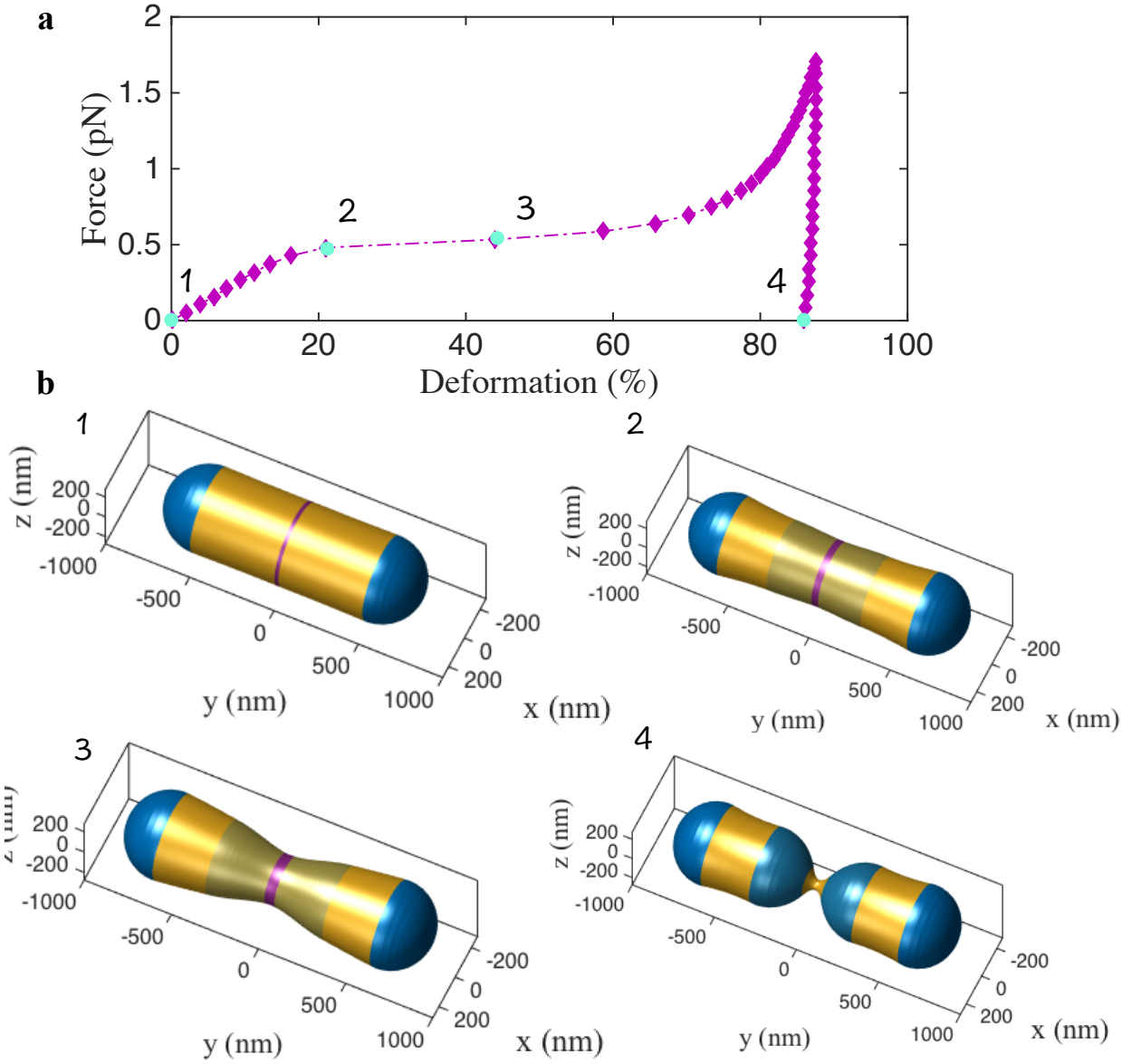

Figure S16: Actin-lipid cooperativity in a mitochondrion with 50% increase in protein area and lipid localization area compared to the system discussed in the main manuscript. The area over which actin applied force reaches a value of 1.3 % of the total area and the area of higher PE concentration domain reaches a value of 6.5 % of the total area. Here, the two areas reach values of 1.95 % and 9.75 % of the total area, respectively. a) The force-deformation response reveals a similar instability as for the spherocylinder discussed in the main manuscript. b) The computed shapes during the force-deformation response.

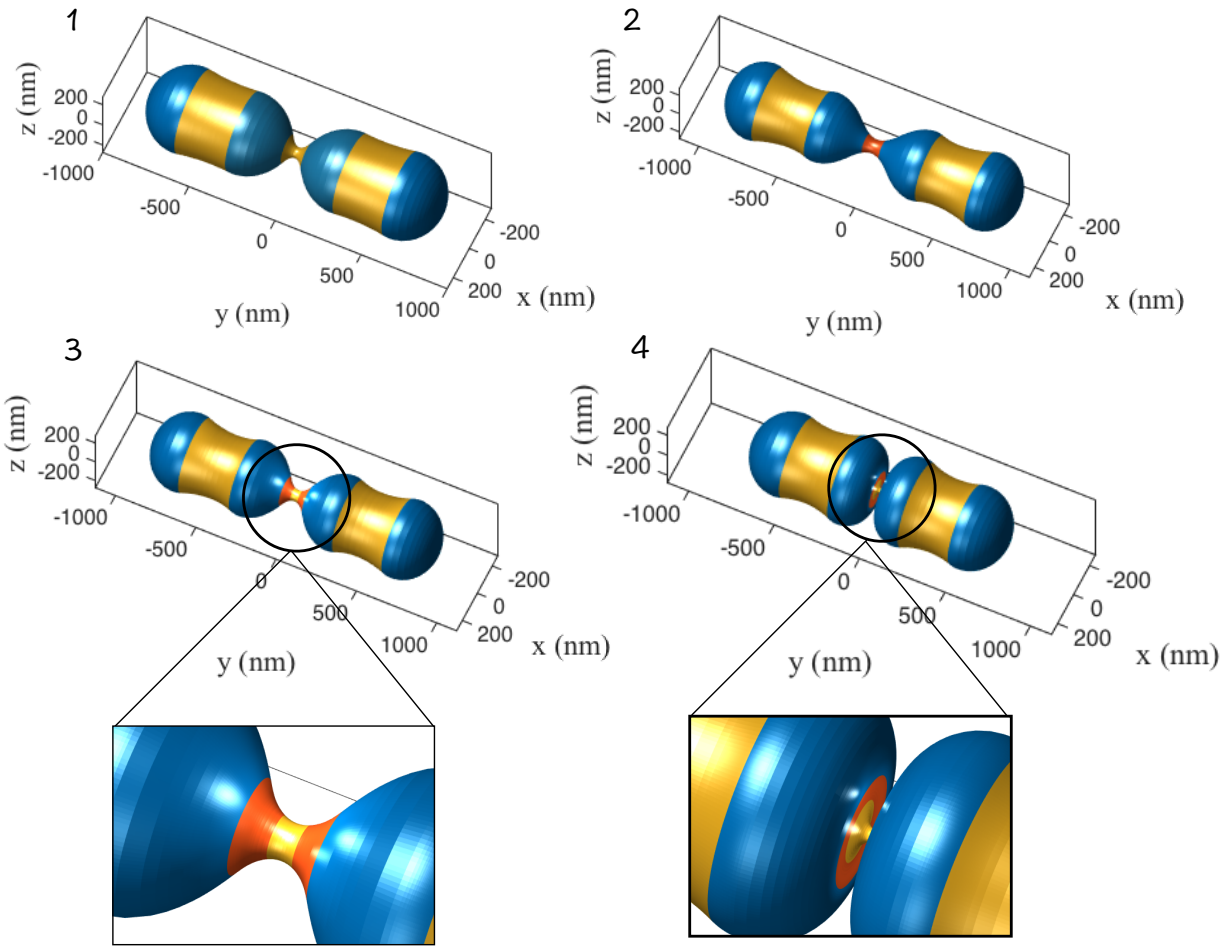

Figure S17: Drp1-lipid cooperativity in a mitochondrion with 50% increase in protein area and lipid localization area compared to the system discussed in the main manuscript. The area over which actin applied force reaches a value of 1.3 % of the total area and the area of higher PE concentration domain reaches a value of 6.5 % of the total area. Here, the two areas reach values of 1.95 % and 9.75 % of the total area, respectively. b) The computed shapes during the polymerization and the splitting phases reveal a similar instability as for the spherocylinder discussed in the main manuscript.

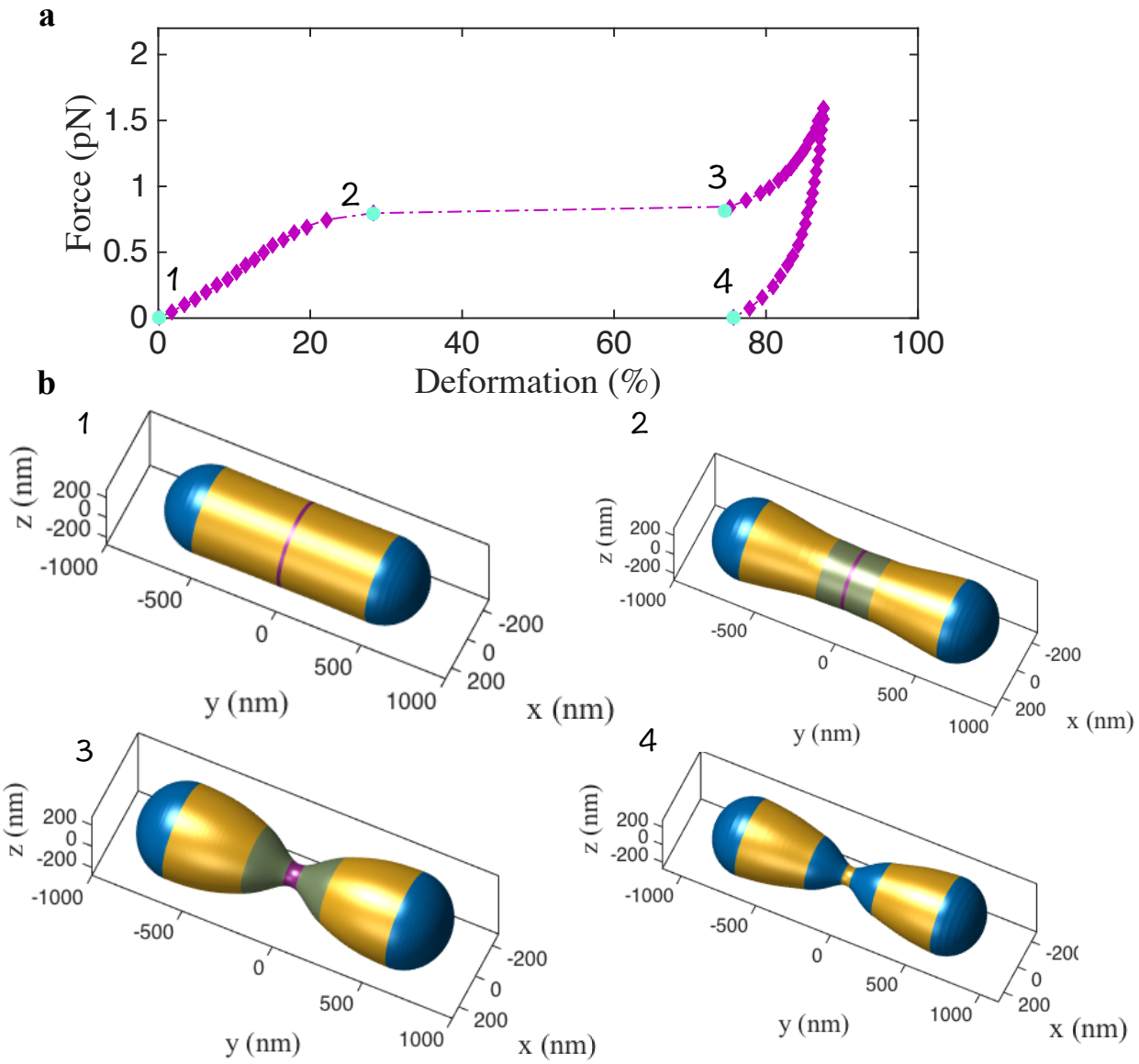

Figure S18: Actin-lipid cooperativity in a mitochondrion with 25% decrease in protein area and lipid localization area compared to the system discussed in the main manuscript. The area over which actin applied force reaches a value of 1.3 % of the total area and the area of higher PE concentration domain reaches a value of 6.5 % of the total area. Here, the two areas reach values of 0.98 % and 4.88 % of the total area, respectively. a) The force-deformation response reveals a similar instability as for the spherocylinder discussed in the main manuscript. b) The computed shapes during the force-deformation response.

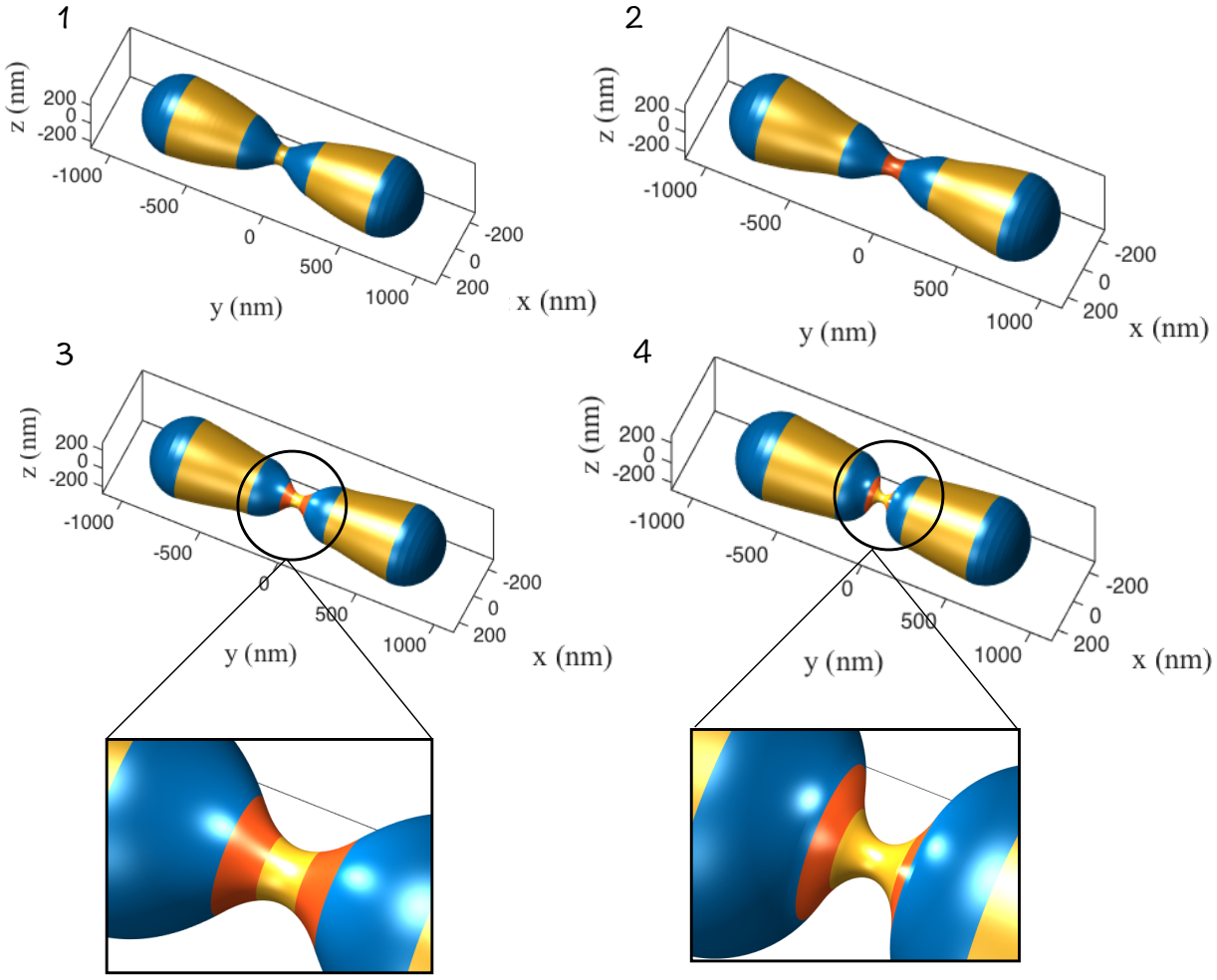

Figure S19: Drp1-lipid cooperativity in a mitochondrion with 25% decrease in protein area and lipid localization area compared to the system discussed in the main manuscript. The area over which actin applied force reaches a value of 1.3 % of the total area and the area of higher PE concentration domain reaches a value of 6.5 % of the total area. Here, the two areas reach values of 0.98 % and 4.88 % of the total area, respectively. The computed shapes during the polymerization and the splitting phases reveal a similar instability as for the spherocylinder discussed in the main manuscript.